Treatment of point-to-point numerical oscillations via local grid refinement

By H. H. A. Xu AND X. I. A. Yang

1. Motivation and objectives

Unphysical numerical oscillations are undesirable artifacts in computational fluid dynamics (CFD) simulations, and they occur when a central difference scheme is used to discretize fluid equations on a coarse grid (Gresho & Lee 1981). For example, let us consider a detached eddy simulation of laminar incoming flow passing a two-dimensional (2D) airfoil, where the near-wall boundary layer is not resolved by the grid. Unphysical oscillations occur at the leading edge when using a coarse grid and a non-dissipative scheme, and the presence of the airfoil directly affects the flow within the oscillation boundary layer, whose wall-normal extent is significantly larger than the boundary-layer thickness of the physical boundary layer. In order to remove such unphysical numerical oscillations, the most straight-forward approach is to increase grid resolution (until all relevant scales are resolved). However, relying solely on grid refinement for dealing with numerical oscillations is often impractical because of the related computational cost. Other commonly used oscillation-suppressing strategies include upwind schemes, artificial viscosity and digital filtering, which, in one way or another, alter the discretized governing equations.

The use of upwind schemes such as the Godunov scheme (Godunov 1959) and the MUSCL scheme (Colella 1985) dates back to the 1960s (Mendu 1959; Guillou *et al.* 1970; Roache & Mueller 1970). However, because of the overly dissipative nature of upwind schemes (Franke & Rodi 1993; Mittal & Moin 1997; Spyropoulos & Blaisdell 1998), in the recent literature, upwinding is used either in confined regions (e.g., near a shock wave (Anderson & Wendt 1995; Laney 1998; Ducros *et al.* 1999)) or with procedures that limit the related numerical dissipation (Bui 2000; Tajallipour *et al.* 2009). The use of artificial viscosity to remove unphysical numerical oscillations has the same pros and cons with upwind schemes (although artificial viscosity can be localized in spectrum space). On one hand, introducing artificial viscosity smooths numerical solutions and stabilizes otherwise-unstable calculations (Tadmor 1989; Russell & Binning 2004; Mani *et al.* 2009); on the other hand, the small-scale features are often destroyed because of the overly dissipative nature of applying artificial viscosity (Turkel & Vatsa 1994; Caramana *et al.* 1998; Cook & Cabot 2004). Yet another strategy to deal with unphysical numerical oscillations is filtering, where solutions at each time step are low-pass filtered to damp high-wave-number oscilelatory modes (Goldstein *et al.* 1993; Tseng *et al.* 2006; Mariano *et al.* 2010). Similar to upwind schemes and artificial viscosity, digital filters also alter the discretized governing equation.

Whenever possible, it is preferable to obtain smooth numerical solutions using non-dissipative schemes without any filtering procedure attached. This consideration leads directly to grid refinement. Unphysical numerical oscillations occur in regions where flow accelerates or decelerates rapidly, and may be removed by refining the mesh within these regions before a calculation (Sabau & Raad 1999) or during a calculation (Yeh 1990; Yeh

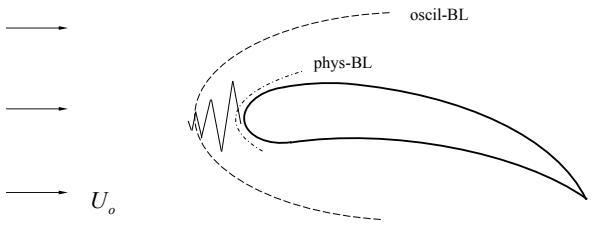

FIGURE 1. A sketch of laminar incoming flow passing a two-dimensional airfoil. Unphysical numerical oscillations occur near the leading edge. A boundary layer may be defined based on the oscillation magnitude, whose height is indicated as oscil-BL. The real boundary layer is indicated as phys-BL.

et al. 1992). The idea is as follows. A coarse grid calculation is conducted first. Then one selectively refines the mesh in regions where numerical oscillations are found. The two steps are repeated until the solution becomes non-oscillatory. Here, the coarse grid calculation may be a good guess of the flow field, in which case, this two-step procedure will need to be applied only once, and the mesh deployment is determined before a real CFD calculation. Alternatively, this procedure can be carried out dynamically during a calculation, in which case mesh refinement is automated. The latter approach is known as adaptive mesh refinement (AMR) (Plewa *et al.* 2005). Compared with upwind schemes, artificial viscosity and digital filters, refining mesh until unphysical oscillations are removed typically leads to more accurate results (Mittal & Moin 1997). However, relying solely on mesh refinement (e.g., AMR) for removing unphysical numerical oscillations can be impractical because of the following two reasons. First, unphysical numerical oscillations are not confined within a small region, but are usually found throughout the entire computational domain. As a result, the entire mesh must be refined, which can be very expensive. Second, because the local grid stretching ratio typically does not exceed two (Iwatsu *et al.* 1989; Johnson & Patel 1999; Beaudan & Moin 1994; Rai & Moin 1991), refining the mesh within one region requires the mesh in the surrounding regions to be refined as well, leading to additional computational cost. In this report, we attempt to resolve these two issues. We will show that once we refine grid at locations where flow decelerates, unphysical numerical oscillations in other regions are automatically removed. We will also show that we may stretch the grid by a factor of $O(10)$ for suppressing unphysical oscillations.

The discussion will focus on numerical oscillations due to rapid flow deceleration in the context of finite-difference/finite-volume methods, and in this work we mainly consider flow acceleration/deceleration in space. Discrete Galerkin methods naturally admit solutions with discontinuities (Bourgeat & Cockburn 1987; Cockburn & Shu 1989; Cockburn *et al.* 1989, 1990; Cockburn & Shu 1998) and therefore are not relevant here. Whether a change in fluid velocity is a deceleration or an acceleration depends on the frame of reference, and therefore we will use flow acceleration and flow deceleration interchangeably. We will also use grid stretching and grid compression interchangeably for the same reason.

The rest of the report is organized as follows. In Section 2, a modal problem is used to motivate our approach. The present grid refinement strategy is further motivated in Section 3. Details of the computational setup are included in Section 4, followed by results in Section 5. Finally, conclusions are given in Section 6.

2. Modal problem

We motivate our approach by considering the following (1D) advection-diffusion equation,

$$c\frac{du}{dx} = \nu\frac{du^2}{dx^2}, \tag{2.1}$$

where u is a generic flow quantity (e.g., the velocity), c is a specified convective velocity and ν is the kinematic viscosity. We consider a 1D domain of unit length with Dirichlet boundary conditions on both ends

$$u(x=0) = 1, \qquad u(x=1) = 0. \tag{2.2}$$

A central difference scheme is used for discretization, where the discretization of both the convective term and the diffusion term attains second-order accuracy on a uniform grid. For a conservative scheme and at a sufficiently high Reynolds number (Re$= L_x c/\nu$, where L_x is the extent of the domain), integrating the discretized energy equation leads to

$$\frac{1}{2}c \cdot u^2(x=0) - \frac{1}{2}c \cdot u^2(x=1) = \Phi\Delta x, \tag{2.3}$$

where Δx is the grid spacing (assuming uniform grid spacing), Φ is the volume-integrated dissipation rate, which is

$$\Phi = \nu\frac{(u_1-u_0)^2 + (u_2-u_1)^2 + ... + (u_n-u_{n-1})^2}{\Delta x^2}, \tag{2.4}$$

where u_i is the solution on the ith grid point, u_0 is at $x=0$ and u_n is at $x=1$. The exact solution of this modal problem is monotonic and non-oscillatory. If a monotonic, non-oscillatory numerical solution of u is to be obtained, the following inequality holds

$$\Phi \leq \nu\frac{(u_0-u_n)^2}{\Delta x^2}. \tag{2.5}$$

Combining Eqs. (2.3) and (2.5), we obtain a necessary condition for a non-oscillatory solution

$$\frac{c}{2} \leq \nu\frac{1}{\Delta x}, \tag{2.6}$$

which then leads to the well-known condition

$$\mathrm{Pe}_\Delta = \frac{c\Delta x}{\nu} \leq 2. \tag{2.7}$$

For this 1D advection-diffusion equation, it is well known that using a uniform grid with $\mathrm{Pe}_\Delta > 2$ leads to unphysical numerical oscillations near $x=1$ (see Figure 2 and Roache (1972); Hirsch (2007)). This conclusion may also be obtained through simple numerical analysis. Here, instead of taking a numerical perspective, we provide a physics-based interpretation for the criterion in Eq. (2.7). According to Eq. (2.3), the convective flux is fixed by boundary conditions, and is balanced by the volume-integrated dissipation rate. For a given grid, the maximum dissipation admitted by a non-oscillatory solution is given by Eq. (2.5), where the equality is attained when all the changes in u are concentrated within one grid cell. Numerical oscillation occurs when this maximum dissipation is not large enough to balance the convective flux.

Following the above arguments, to prevent unphysical oscillations, we must allow a non-oscillatory solution to generate sufficient dissipation, which may be done by introducing additional numerical dissipation, or simply by adding one refined grid at the location where flow decelerates, i.e., by decreasing Δx in Eq. (2.5). This is the grid refinement

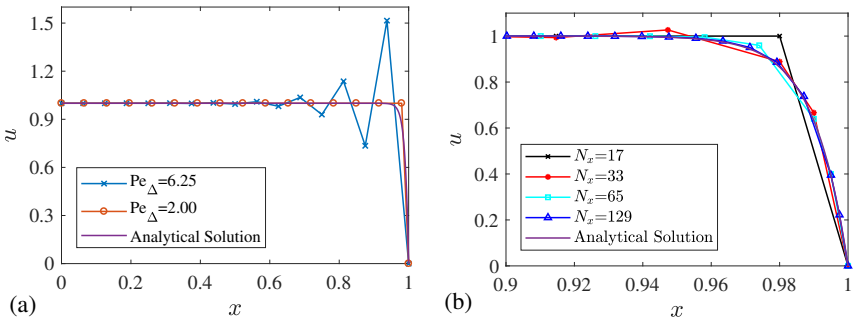

FIGURE 2. (a) Numerical solution obtained on a nonuniform grid with the cell Peclet number $\mathrm{Pe}_\Delta = 2$ near the right boundary (case $\mathrm{Pe}_\Delta = 2.00$), and results on a uniform grid with the same number of grid points (denoted as $\mathrm{Pe}_\Delta = 6.25$). The analytical solution $\exp(\mathrm{Re}\ x)/[1-\exp(\mathrm{Re})]+\exp(\mathrm{Re})/[\exp(\mathrm{Re})-1]$ is included for comparison, where $\mathrm{Re} = L_x c/\nu$. (b) Numerical solution obtained through refining the grid from $\mathrm{Pe}_\Delta = 2$ case in (a) (corresponding to $N_x = 17$) three times by inserting mid points between any two nodes from previous grid and analytical solution is also plotted for comparison.

strategy proposed here: if the sole purpose is to obtain a non-oscillatory solution (to remove the unphysical numerical oscillations), one only needs to add one refined layer of grid at locations where flow velocity changes rapidly—the numerical solution would then concentrate all the velocity gradients within that refined cell. Whether the solution would follow our expectation and concentrate most of its gradients into the one refined grid cell is not guaranteed.

To test the usefulness of this grid refinement strategy, we solve Eq. (2.1) numerically on a non-uniform grid with 16 grid points. $\nu = 0.01$, $c = 1$ and $\Delta x = 0.0653$ for $i = 1$ to 15. For the last grid point near $x = 1$, $\Delta x_{16} = 0.02$ is used, and $\mathrm{Pe}_\Delta = 2$ at that last grid. The results are shown in Figure 2(a). The solution is non-oscillatory, and all the gradients are indeed within the last computational cell, leading to just enough dissipation within the domain to balance the convective flux. The exact solution and the numerical solution obtained on a uniform mesh are also included for comparison. A few observations can be made. First, unphysical numerical oscillations are found when a uniform grid with $\mathrm{Pe}_\Delta > 2$ is used (as expected), and oscillations are found to be approximately nine grid points upstream of $x = 1$. Second, the dominant wavelength of the oscillatory modes spans two grid points. Therefore, unphysical numerical oscillations are not admissible to standard large-eddy simulation (LES) subgrid models (Germano *et al.* 1991; Meneveau *et al.* 1996). Hence unphysical oscillations may be present also in Reynolds-averaged Navier-Stokes calculations and LES. Third, adding one refined grid at the location where flow decelerates removes oscillations within the entire domain. Fourth, although it is trivial, it is worth noting that a solution with no unphysical numerical oscillations is not necessarily an accurate solution. Consider again the case sketched in Figure 1. The present strategy is only meant to remove the unphysical oscillation boundary layer. If the physical boundary layer near the airfoil and the related momentum loss at the wall are to be captured, more grid points must be used in the near-wall region (for direct computation), or a near-wall closure must be employed. This point is also clear from Figure 2(b), where the solution of Eq. 2.1 is obtained only when more grid points are used near $x = 1$ (i.e., refining beyond $\mathrm{Pe}_\Delta = 2$). High-order schemes are advantageous over low-order schemes only when the oscillations are removed.

The results are encouraging (as long as we focus on removing the unphysical numer-

ical oscillations). However, the usefulness of this grid refinement strategy in real-world problems has yet to be tested. In addition, even this grid refinement strategy applies equally effectively to real-world engineering problems, knowing *a priori* where flow velocity changes rapidly is not always straight-forward. Below, we will show the usefulness of this mesh refinement strategy for a few simple flows. It is also clear that for many cases, it is in fact not difficult to guess where flow decelerates.

3. Present grid refinement strategy

In the preceding section, we used a 1D advection diffusion equation to motivate the present approach of grid refinement for removing unphysical numerical oscillations. Following the discussion in the preceding section, here we estimate the grid stretching/compression ratio that one would typically encounter when applying this strategy. Without loss of generality, we consider rapid flow deceleration. Within the refined cell, we also write the energy equation Eq. (2.3). The dissipation is given by $\Phi_\Delta \Delta x = \nu \Delta u^2/\Delta x$, where Φ_Δ is the dissipation within that refined cell, Δu is the deceleration, and Δx is the size of the cell. The advection is given by $\Pi = 0.5\Delta u^3$ (here we choose a frame of reference according to which flow decelerates to zero). $\Phi_\Delta \Delta x \geq \Pi$ for a non-oscillatory solution, which gives

$$\Delta x_r \leq \frac{2\nu}{\Delta u}. \tag{3.1}$$

Elsewhere we will use coarse grids, where a characteristic length L is resolved by N grid points. Hence the grid stretching/compression ratio near the refined grid is

$$r = \frac{L/N}{\Delta x_r} \geq \frac{\mathrm{Re}}{2N}\frac{\Delta u}{U} = \frac{\Delta u}{2U}\mathrm{Pe}_\Delta, \tag{3.2}$$

where U is the characteristic velocity of the flow and $\mathrm{Re}= LU/\nu$ is the bulk Reynolds number. We make two observations. First Eq. (3.2) indicates that to effectively suppress numerical oscillations, r increases as the cell Peclet number increases. This is expected because for a better resolved calculation, a less aggressive local mesh refinement would be needed to suppress the oscillations. Second, Eq. (3.2) indicates that r decreases as a function of $\Delta u/U$. This ratio is $O(0.01)$ for a well-resolved calculation. This ratio will be much larger for a coarse calculation, indicating, again, that for a better-resolved calculation, a less aggressive local refinement is needed. In anticipation of the results below (flow configuration A1), $\Delta u/U \approx 0.15$, $\mathrm{Re}= 4000$, $N = 64$, and Eq. (3.2) gives $r > 4.7$ for an effective suppression of unphysical numerical oscillations. This prediction is in fact not very far from the empirically observed value. For typical CFD calculations where $\mathrm{Pe}_\Delta \approx 100$ and $\Delta u/U \approx 0.1$, a local refinement of approximately $r \gtrsim 5$ would be needed at locations where flow velocity changes rapidly. Thus the present grid refinement strategy may require $r \gg 1$, while the commonly used stretching ratio r does not exceed two. Last, we note that Eq. (3.2) is but a rough estimate.

4. Tests

The usefulness of the proposed grid refinement strategy is tested in this section. The in-house incompressible Navier-Stoke solver ViCar3D is used for the cases in this section. This code has been extensively used for fluid flow problems (Luo *et al.* 2008; Yang *et al.* 2016; Sadique *et al.* 2017; Yang & Meneveau 2017). Here we briefly summarize the main

features of the code. A sharp-interface immersed boundary method (Mittal & Iaccarino 2005; Mittal *et al.* 2008) is used to resolve solid bodies within the flow field. Spatial discretization is based on a second-order central finite difference scheme, and the projection method is employed for time discretization. Flow configurations are detailed in Section 4.1, and the results are presented in Section 4.2. We will mainly consider steady and quasi-steady flows. It is worth noting that unphysical oscillations appear also in turbulent flows (e.g., atmospheric boundary layers over urban canopies, where unphysical oscillations are found upstream of urban buildings). However, unphysical oscillations in turbulent flows are most visible in the mean flow, where time averaging would have already removed the unsteady turbulence. In other words, studying the problem of unphysical oscillations in a turbulent context means studying a numerical solution that is composed of unphysical mean oscillations, physical mean flow and unsteady turbulence, where turbulence itself does not play an important role.

4.1. *Setup*

The first flow configuration we use for testing is the 2D lid-driven cavity. The flow configuration is sketched in Figure 3(a). The flow is driven by the top lid, which is at a constant velocity U_l. The cavity is of size $L_l \times L_l$. Flow accelerates and decelerates rapidly near the left ($x = 0$) and the right ($x = L_l$) boundaries. Therefore, a refined grid is added to each side (see Figure 3(b) for a sketch of the mesh). The effects of Reynolds number and grid resolution will be investigated. The proposed grid refinement strategy is found to be robust and provides non-oscillatory solutions for all Reynolds numbers and all resolutions. A three dimensional (3D) lid-driven cavity is included as the second test flow configuration, where a uniform grid is used in the spanwise direction. For brevity, results at only one Reynolds number are shown in this section, and we refer to this case as B1. The third and fourth test flow configurations are flow passing a wall-mounted cube (Figure 4(a)) and uniform incoming flow passing a cube (Figure 5(a)), which we refer to as C1 and D1, respectively. In both cases, the cube is of size L_c^3 and locates at the center of the spanwise and the streamwise dimension. The computational domain is $8L_c \times 4L_c \times 4L_c$ in the streamwise, wall-normal and the spanwise directions. A periodic boundary condition is imposed in the spanwise direction, and a standard outflow condition is used at the outlet. For the wall-mounted cube case, a no-slip condition is used for both the bottom and the top boundaries. As for the other case, a Dirichlet condition, $u = U_o$, is imposed on the top and bottom boundaries. The flow is expected to decelerate rapidly upstream of the cube and a refined grid is added just upstream of the cube [see sketches of the grid deployment in Figures 4(b), 5(b)].

Other details of the test cases are summarized in Table 4.1. The grid spacing is uniform in all directions except for one refined layer as mentioned above. The local grid stretching/compression ratio is

$$r = \frac{\Delta_{\text{uniform}}}{\Delta_{\text{thin}}}, \tag{4.1}$$

where Δ_{uniform} is the grid spacing in the streamwise direction in the regions where the grid is uniformly spaced, and Δ_{thin} is the size of the refined layer. For two runs of the same flow configuration but with two different values of r, the grid spacing in regions where the mesh is uniform is slightly different so that the total number of grid points can be kept unchanged. We will show first that, at the listed Reynolds numbers with the listed grid points, the solutions are plagued with unphysical numerical oscillations when

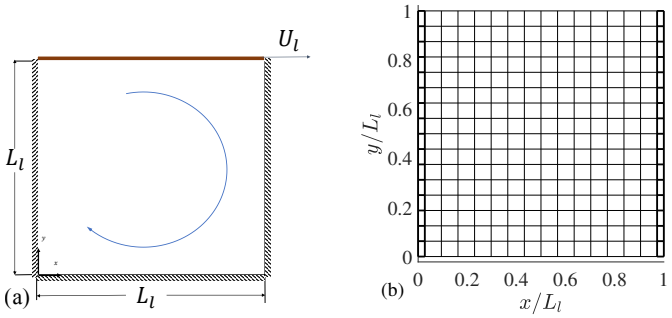

FIGURE 3. (a) A sketch of the 2D lid-driven cavity. (b) A sketch of the mesh in the $x-y$ plane with $N_x = N_y = 16$ and $r = 2.5$. r is the local grid refinement ratio and is defined in Eq. (4.1). The refined layer is highlighted using thicker lines.

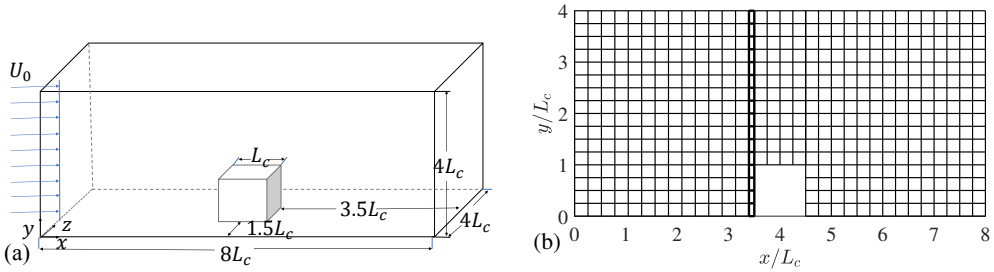

FIGURE 4. (a) A sketch of flow passing a wall-mounted cube. U_0 is the velocity of the incoming flow. (b) A sketch of the $x-y$ plane mesh through the center of the spanwise dimension. For the sketch shown here $N_x = 32, N_y = N_z = 16$ and $r = 2.5$. The refined layer is highlighted using thicker lines. The mesh is uniform in the spanwise (z) direction.

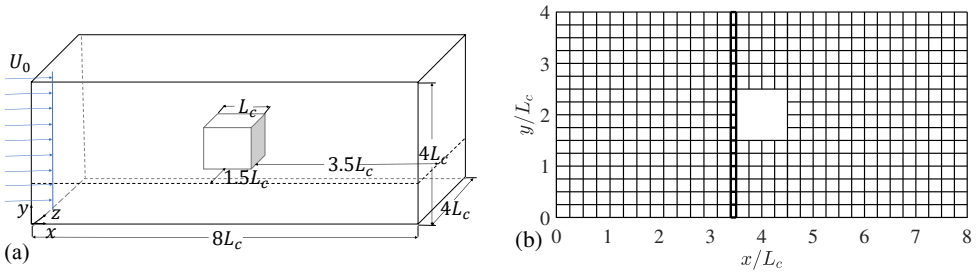

FIGURE 5. (a)A sketch of flow passing a cube. (b)Same as Figure 4(b) but for flow passing a cube.

a uniform mesh is used, and, second, that the oscillations can be removed by refining one grid at regions where flow decelerates.

4.2. *Oscillation quantification*

For the test cases considered, unphysical numerical oscillations are most prominent in the streamwise velocity component. We thus start by considering streamwise velocity as a function x, i.e., $u(x)$, which contains both the desired solution and unphysical numerical oscillations. Instead of the entire streamwise (x) extent, we focus on the streamwise extent where numerical oscillations are prominent. For cases A1, A2 and B1, this extent is from

Case	Re	N_x	N_y	N_z
A1	4000	64	64	-
A2	8000	128	128	-
B1	4000	64	64	64
C1	500	64	32	32
D1	500	64	32	32

TABLE 1. Simulation details. N_i is the number of grid points in ith Cartesian direction. The Reynolds number is defined as Re= $L_l U_l/\nu$ for lid-driven cavity flows (A1, A2, B1), and is Re= $L_c U_0/\nu$ for flow passing a cube (C1, D1).

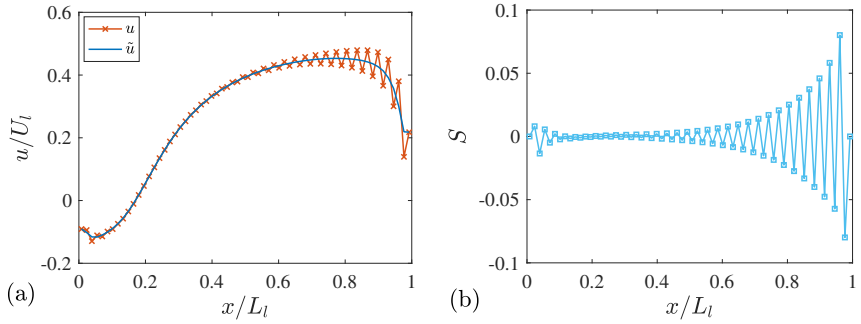

FIGURE 6. (a) A sample of an oscillatory solution u and the desired solution $\tilde{u}$. (b) Numerical oscillation $S(x) = u(x) - \tilde{u}(x)$.

$x = 0$ to $x = L_l$, and for cases C1 and D1, this extent is from the inlet to the front surface of the cube, i.e., from $x = 0$ to $x = 3.5L_c$ (see Figures 4 and 5). The desired solution can be obtained by filtering the numerical solution $u(x)$ (which is also the starting point of approaches that rely on digital filtering for removing oscillations).

Because the wavelength of the dominant oscillatory mode spans two grid points, the filter used here is a weighted digital filter in physical space with the weight $[1/4, 1/2, 1/4]$ (i.e., $\tilde{u}_i = 1/4u_{i-1} + 1/2u_i + 1/4u_{i+1}$). We define $\tilde{u}(x)$ to be the physical solution, and it follows that $S(x) = u(x) - \tilde{u}(x)$, which is a signal of unphysical numerical oscillations. A sample of $u(x)$, $\tilde{u}(x)$ and $S(x)$ is sketched in Figure 6, where the three signals are shown as functions of the spatial coordinate x. This decomposition procedure is used only to quantify the strength of unphysical oscillations, and is not used for removing the oscillations within a calculation.

The strength of unphysical oscillations is quantified using the volume-averaged total variation of $S(x)$. The total variation of a discretized signal S_i can be computed as follows

$$T_v = \frac{1}{U_n} \sum_{i=n_{x_1}}^{i=n_{x_2}} |S_{i+1} - S_i| , \tag{4.2}$$

where U_n is a normalizing velocity and indexes n_{x_1} and n_{x_2} depend on the streamwise extent of interest. The normalizing velocity is $U_n = C[\max(\tilde{u}) - \min(\tilde{u})]$. We set $C = 2$ for lid-driven cavity flow and $C = 1$ for flow passing a cube (considering the flow in a cavity

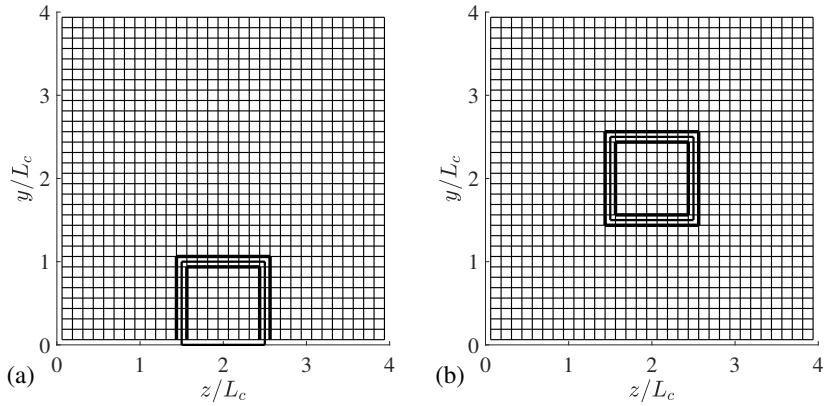

FIGURE 7. (a) Region of interest for case C1, highlighted in thick lines. (b) Same as (a) but for case D1.

is at rest at $x = 0$, finite within the domain and then at rest again at $x = 1$, but the flow in cases C1 and D1 is U_0 at the inlet and monotonically decreases to zero at the cube front surface). The volume-averaged total variation of $S(x)$ is obtained by integrating T_v for y and z locations of interest and then normalizing by the $y - z$ integrated area. We will denote this volume-averaged quantity as follows,

$$\zeta = \frac{1}{S_{yz}} \int \int T_v dy dz. \tag{4.3}$$

The y, z locations of interest are comprised of the top four layers of the grids for cases A1, A2, B1, and comprise of the regions indicated in Figure 7 for cases C1 and D1.

5. Results

It follows from Section 3 that the present grid refinement strategy leads to $r \gg 1$. To quantify the effects of grid stretching on numerical oscillations, for each flow configuration in Section 4.1, a series of calculations are performed where we vary r from 1 to ≈ 10. Since it is unlikely that grid stretching $r > 10$ would be of any practical use, $r > 10$ is not considered. $r = 1$ corresponds to a uniform coarse grid, where the solution is plagued with unphysical numerical oscillations. Results of the lid-driven cavity flow are shown in Section 5.1, and results of flow passing a cube are shown in Section 5.2.

5.1. *Lid-driven cavity*

Figure 8 shows ζ as functions of the grid stretching ratio for configurations A1 and A2 (2D lid-driven cavity). We have kept the mean cell Peclet number unchanged between cases for configurations A1 and A2. The difference between the measured ζ functions therefore arises solely because of the Reynolds number. A steady-state solution cannot be obtained for $1 < r < 2$ for configuration A2 (see Ghia *et al.* (1982); Erturk (2009) for detailed discussion on the effect of grid deployment on 2D lid-driven cavity flow). We make a few observations. First, the grid refinement strategy effectively suppresses unphysical numerical oscillations. ζ decreases as r increases until some optimal value and then increases slightly. Second, $\zeta > 0$ and is never 0. Hence, 2-Δx waves are never completely removed from the simulation. This is probably a desirable feature because a typical flow admits modes at all wave numbers and it is only when the energy within

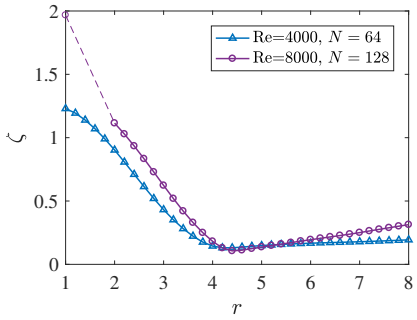

FIGURE 8. The strength of unphysical numerical oscillations ζ as functions the grid stretching ratio r for a 2D lid-driven cavity with Re= 4000 and Re= 8000. $N = N_x = N_y$ is the grid point in one of the Cartesian directions. Each data point represents a calculation.

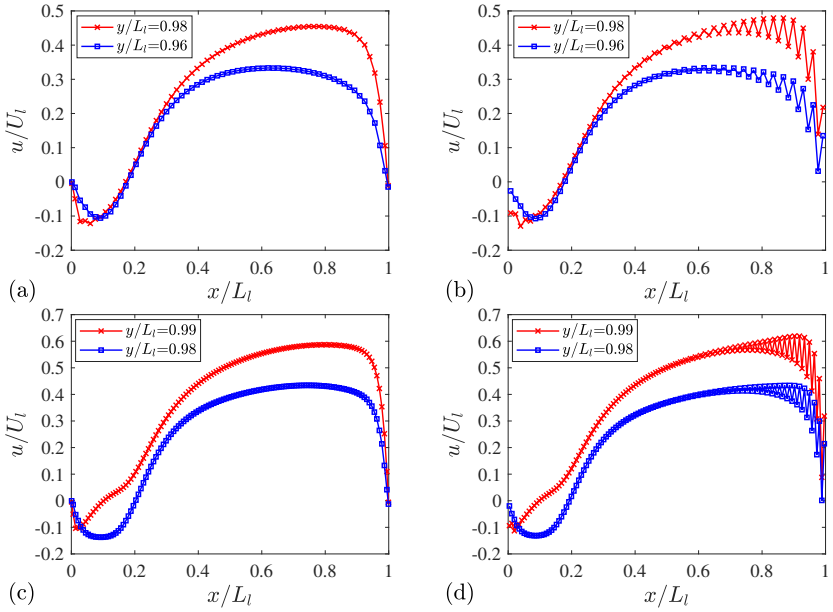

FIGURE 9. (a) Streamwise velocity profile along x for configuration A1 at two y locations. $r = 4.4$. (b) Streamwise velocity profile along x for configuration A1. $r = 1$. (c) Same as (a) but for configuration A2 (d) Same as (b) but for configuration A2.

the 2-Δx mode is excessively large can this mode be considered as unphysical numerical oscillations. Third, for two flows that are equally resolved (with the same mean cell Peclet number), unphysical numerical oscillations are more prominent for flows at a higher Reynolds number.

Figure 9(a-d) shows the streamwise velocity as functions of x/L_l for cases A1 and A2. The unphysical numerical oscillations are effectively suppressed through the addition of a refined layer next to the two vertical walls.

Figure 10(a-f) shows the streamwise velocity along x/L_l at three spanwise locations $z/L_l = 0.01, 0.24$, and 0.49 (results are symmetric with respect to $z/L_l = 0.5$) for configuration B1 with $r = 3.5$ and $r = 1$. Again, for 3D lid-driven cavity flow, unphysical numerical oscillations are also suppressed through the addition of one refined layer to the two vertical walls in the x direction.

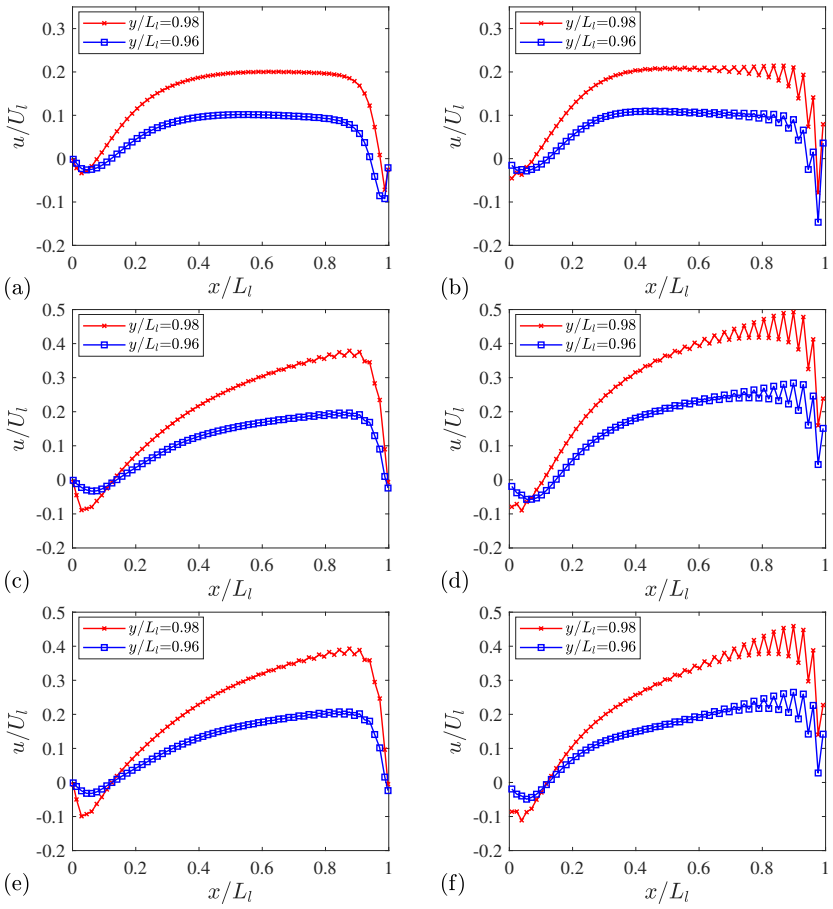

FIGURE 10. (a) Streamwise velocity profile along x at the spanwise location $z/L_l = 0.01$ and two y locations for case B1, $r = 3.5$. (b) Same as (a) but for $r = 1$. (c) Same as (a) but at the spanwise location $z/L_l = 0.24$. (d) Same as (c) but for $r = 1$. (e) Same as (a) but at the spanwise location $z/L_l = 0.49$. (f) Same as (e) but for $r = 1$.

5.2. *Flow passing a cube*

Figure 11(a, b) shows ζ as functions of r for configurations C1 and D1. Cases C1 and D1 give very similar results (the exact magnitude of ζ is not very relevant here). The strength of unphysical numerical oscillations decreases as a function of r for $r \gtrsim 2$. Numerical oscillations are effectively suppressed for $r \gtrsim 6$. Again, ζ is not zero for any r. Figure 12(a-d) shows the streamwise velocity as functions of x/L_c at a few y and z locations. We compare results at $r > 6$ and at $r = 1$. Again, the results of cases C1 and D1 are very similar. We make a few observations. First, the numerical solution on a uniform grid is plagued with unphysical numerical oscillations. The oscillations are so strong that the acceleration of fluid around the cube is not even discernible. Second, numerical oscillations are present not only near the cube (the front surface of the cube is at $x/L_c = 3.5$), but also at the inlet. Third, the oscillations are greatly suppressed when a refined layer is added in front of the cube, but they are not completely removed. Fourth, while not shown here, refining the grid near the other cube surfaces leads to slightly improved results (ζ drops from ≈ 3 to ≈ 2). Given that such geometries are quite

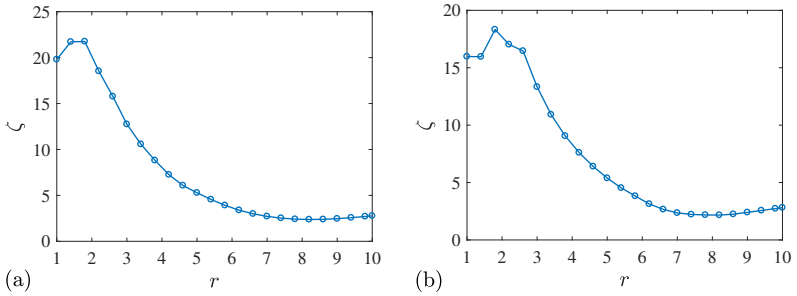

FIGURE 11. (a) Strength of unphysical numerical oscillation ζ as a function of r for flow passing a wall mounted cube (case C1). (b) Same as (a) but for case D1.

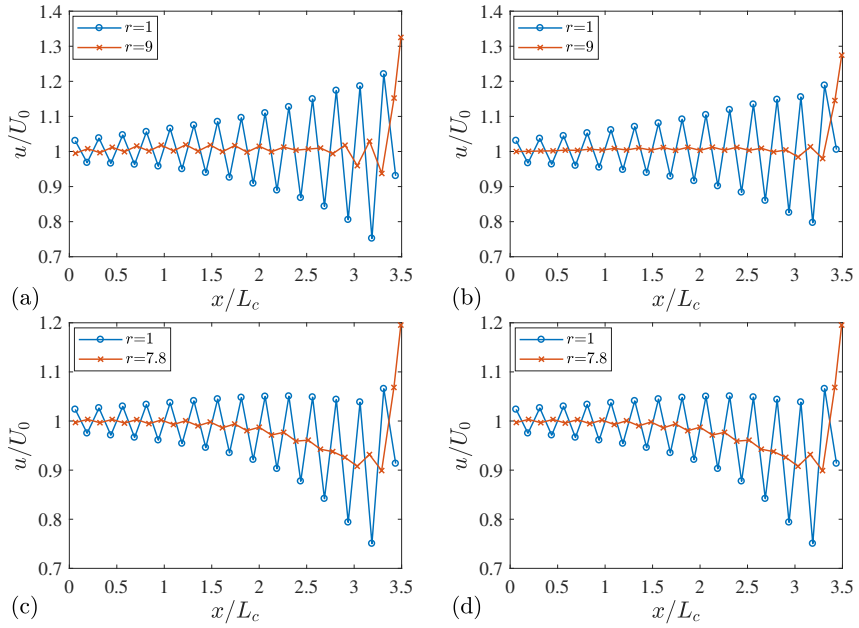

FIGURE 12. (a) Streamwise velocity profiles along x at $y/L_c = 0.56$ and $z/L_c = 1.44$ for two grid stretching ratios $r = 1$ and $r = 9$. Results of case C1 are shown. (b) Same as (a) but at $y/L_c = 0.81$ and $z/L_c = 2.56$. (c) Streamwise velocity profile along x at $y/L_c = 1.69$ and $z/L_c = 1.44$ for two grid stretching ratios $r = 1$ and $r = 7.8$. Results of case D1 are shown. (d) Same as (c) but at $y/L_c = 2.31$ and $z/L_c = 2.56$.

common in urban canopies (Tseng *et al.* 2006; Coceal *et al.* 2007; Xie & Castro 2006), the discussion in this subsection may be quite relevant for CFD calculations of urban boundary layers.

6. Conclusions

In this work, we have proposed a local mesh refinement strategy for removing unphysical numerical oscillations. We have shown that these unphysical oscillations are effectively suppressed by adding a single refined grid at locations where flow velocity changes rapidly, without the aid of artificial/numerical viscosities within the computational domain. The present strategy leads to a grid stretching/compression ratio $r \gg 1$,

and we have shown such an aggressive mesh refinement is in fact not problematic. The proposed method is tested for a few 2D and 3D steady and quasi-steady flows. As numerical oscillations also persist in a turbulent environment (which can be found in the mean flow), the discussion is also relevant for turbulent flows. The results improve as Reynolds number increases and from 2D cases to 3D cases, showing much promise for real-world engineering problems (although those problems do not provide a clean environment for testing the present strategy). However, we note that introducing a refined grid restricts the size of time stepping and therefore leads to computational over-head. Nonetheless, this would probably be less of a problem if one uses implicit time stepping (Mansour & Hamed 1990; Luo *et al.* 1994).

Acknowledgments

This investigation is funded by AFOSR, Grant #1194592-1-TAAHO. The second author thanks R. Mittal for fruitful discussions.

REFERENCES

Anderson, J. D. & Wendt, J. 1995 *Les. Houch. S.*, vol. 206. Springer.

Beaudan, P. & Moin, P. 1994 *Numerical experiments on the flow past a circular cylinder at sub-critical Reynolds number.* Tech. Rep. #TF-62. Stanford University, Thermosciences Division.

Bourgeat, A. & Cockburn, B. 1987 *The TVD-projection method for solving implicit numeric schemes for scalar conservation laws: A numerical study of a simple case.* IMA Preprint Series #311, University of Minnesota.

Bui, T. T. 2000 A parallel, finite-volume algorithm for large-eddy simulation of turbulent flows. *Comput. Fluids* **29**, 877–915.

Caramana, E. J., Shashkov, M. J. & Whalen, P. P. 1998 Formulations of artificial viscosity for multi-dimensional shock wave computations. *J. Comput. Phys.* **144**, 70–97.

Coceal, O., Dobre, A., Thomas, T. & Belcher, S. 2007 Structure of turbulent flow over regular arrays of cubical roughness. *J. Fluid Mech.* **589**, 375–409.

Cockburn, B., Hou, S. & Shu, C. W. 1990 The Runge-Kutta local projection discontinuous Galerkin finite element method for conservation laws. IV. The multidimensional case. *Math. Comput.* **54**, 545–581.

Cockburn, B., Lin, S. Y. & Shu, C. W. 1989 TVB Runge-Kutta local projection discontinuous Galerkin finite element method for conservation laws. III. One-dimensional systems. *J. Comput. Phys.* **84**, 90–113.

Cockburn, B. & Shu, C. W. 1989 TVB Runge-Kutta local projection discontinuous galerkin finite element method for conservation laws. II. General framework. *Math. Comput.* **52**, 411–435.

Cockburn, B. & Shu, C.-W. 1998 The Runge-Kutta discontinuous Galerkin method for conservation laws V. Multidimensional systems. *J. Comput. Phys.* **141**, 199–224.

Colella, P. 1985 A direct Eulerian MUSCL scheme for gas dynamics. *SIAM J. Sci. Stat. Comp.* **6**, 104–117.

Cook, A. W. & Cabot, W. H. 2004 A high-wavenumber viscosity for high-resolution numerical methods. *J. Comput. Phys.* **195**, 594–601.

Ducros, F., Ferrand, V., Nicoud, F., Weber, C., Darracq, D., Gacherieu, C.

& Poinsot, T. 1999 Large-eddy simulation of the shock/turbulence interaction. *J. Comput. Phys.* **152**, 517–549.

Erturk, E. 2009 Discussions on driven cavity flow. *Int. J. Numer. Meth. Fl.* **60**, 275–294.

Franke, R. T. & Rodi, W. 1993 Calculation of vortex shedding past a square cylinder with various turbulence models. In *Turbulent Shear Flows 8*, pp. 189–204. Springer.

Germano, M., Piomelli, U., Moin, P. & Cabot, W. H. 1991 A dynamic subgrid-scale eddy viscosity model. *Phys. Fluids.* **3**, 1760–1765.

Ghia, U., Ghia, K. N. & Shin, C. 1982 High-Re solutions for incompressible flow using the Navier-Stokes equations and a multigrid method. *J. Comput. Phys.* **48**, 387–411.

Godunov, S. K. 1959 A difference method for numerical calculation of discontinuous solutions of the equations of hydrodynamics. *Matematicheskii Sbornik* **89**, 271–306.

Goldstein, D., Handler, R. & Sirovich, L. 1993 Modeling a no-slip flow boundary with an external force field. *J. Comput. Phys.* **105**, 354–366.

Gresho, P. M. & Lee, R. L. 1981 Don't suppress the wiggles—they're telling you something! *Comput. Fluids* **9**, 223–253.

Guillou, S., Popovics, B. & Nguyen, K. 1970 Numerical simulation of water circulation in marinas of complex geometry by a multi-block technique. *Trans. Built Env.* **43**, 1-10.

Hirsch, C. 2007 *Numerical Computation of Internal and External Flows: The Fundamentals of Computational Fluid Dynamics*. Butterworth-Heinemann.

Iwatsu, R., Ishii, K., Kawamura, T., Kuwahara, K. & Hyun, J. M. 1989 Numerical simulation of three-dimensional flow structure in a driven cavity. *Fluid Dyn. Res.* **5**, 173–189.

Johnson, T. A. & Patel, V. C. 1999 Flow past a sphere up to a Reynolds number of 300. *J. Fluid Mech.* **378**, 19–70.

Laney, C. B. 1998 *Computational Gas Dynamics*. Cambridge University Press.

Luo, H., Baum, J. D., Löhner, R. & Cabello, J. 1994 Implicit schemes and boundary conditions for compressible flows on unstructured meshes. *AIAA Paper* #1994-0816.

Luo, H., Mittal, R., Zheng, X., Bielamowicz, S. A., Walsh, R. J. & Hahn, J. K. 2008 An immersed-boundary method for flow–structure interaction in biological systems with application to phonation. *J. Comput. Phys.* **227**, 9303–9332.

Mani, A., Larsson, J. & Moin, P. 2009 Suitability of artificial bulk viscosity for large-eddy simulation of turbulent flows with shocks. *J. Comput. Phys.* **228**, 7368–7374.

Mansour, M. L. & Hamed, A. 1990 Implicit solution of the incompressible Navier-stokes equations on a non-staggered grid. *J. Comput. Phys.* **86** (1), 147–167.

Mariano, F. P., Moreira, L. d. Q., Silveira-Neto, A. d., da Silva, C. B. & Pereira, J. C. 2010 A new incompressible Navier-Stokes] solver combining fourier pseudo-spectral and immersed boundary methods. *CEMS-Comp. Model. Eng.* **59**, 181–216.

Mendu, L. 1959 Computation of fluid flow with multi-grid and multi-block algorithms. Ph.D. thesis, Texas Tech University.

Meneveau, C., Lund, T. S. & Cabot, W. H. 1996 A Lagrangian dynamic subgrid-scale model of turbulence. *J. Fluid Mech.* **319**, 353–385.

Mittal, R., Dong, H., Bozkurttas, M., Najjar, F., Vargas, A. & von

Loebbecke, A. 2008 A versatile sharp interface immersed boundary method for incompressible flows with complex boundaries. *J. Comput. Phys.* **227**, 4825–4852.

Mittal, R. & Iaccarino, G. 2005 Immersed boundary methods. *Annu. Rev. Fluid Mech.* **37**, 239–261.

Mittal, R. & Moin, P. 1997 Suitability of upwind-biased finite difference schemes for large-eddy simulation of turbulent flows. *AIAA J.* **35**, 1415–1416.

Plewa, T., Linde, T. & Weirs, V. G. 2005 Adaptive mesh refinement-theory and applications. *Lect. Notes Comp. Sci* **41**, 3–5.

Rai, M. M. & Moin, P. 1991 Direct simulations of turbulent flow using finite-difference schemes. *J. Comput. Phys.* **96**, 15–53.

Roache, P. J. 1972 *Computational Fluid Dynamics*. Hermosa publishers.

Roache, P. J. & Mueller, T. J. 1970 Numerical solutions of laminar separated flows. *AIAA J.* **8**, 530–538.

Russell, T. F. & Binning, P. 2004 Oh no, not the wiggles again! A revisit of an old problem and a new approach. *Dev. Water Sci.* **XY 55**, 483–494.

Sabau, A. S. & Raad, P. E. 1999 Oscillations in high-order finite difference solutions of stiff problems on non-uniform grids. *Int. J. Numer. Meth. Fl.* **30**, 939–956.

Sadique, J., Yang, X. I. A., Meneveau, C. & Mittal, R. 2017 Aerodynamic properties of rough surfaces with high aspect-ratio roughness elements: Effect of aspect ratio and arrangements. *Bound-lay. Meteorol.* **163**, 203–224.

Spyropoulos, E. T. & Blaisdell, G. A. 1998 Large-eddy simulation of a spatially evolving supersonic turbulent boundary-layer flow. *AIAA J.* **36**, 1983–1990.

Tadmor, E. 1989 Convergence of spectral methods for nonlinear conservation laws. *SIAM J. Numer. Anal.* **26**, 30–44.

Tajallipour, N., Owlam, B. B. & Paraschivoiu, M. 2009 Self-adaptive upwinding for large eddy simulation of turbulent flows on unstructured elements. *J. Aircraft* **46**, 915-926.

Tseng, Y.-H., Meneveau, C. & Parlange, M. B. 2006 Modeling flow around bluff bodies and predicting urban dispersion using large eddy simulation. *Environ. Sci. Technol.* **40**, 2653–2662.

Turkel, E. & Vatsa, V. N. 1994 Effect of artificial viscosity on three-dimensional flow solutions. *AIAA J.* **32**, 39–45.

Xie, Z. & Castro, I. P. 2006 LES and RANS for turbulent flow over arrays of wall-mounted obstacles. *Flow Turbul. Combust.* **76**, 291–312.

Yang, X. I. A. & Meneveau, C. 2017 Modelling turbulent boundary layer flow over fractal-like multiscale terrain using large-eddy simulations and analytical tools. *Philos. Trans. R. Soc. A* **375**, 20160098.

Yang, X. I. A., Sadique, J., Mittal, R. & Meneveau, C. 2016 Exponential roughness layer and analytical model for turbulent boundary layer flow over rectangular-prism roughness elements. *J. Fluid Mech.* **789**, 127–165.

Yeh, G. 1990 A Lagrangian-Eulerian method with zoomable hidden fine-mesh approach to solving advection-dispersion equations. *Water Resour. Res.* **26**, 1133–1144.

Yeh, G.-T., Chang, J.-R. & Short, T. E. 1992 An exact peak capturing and oscillation-free scheme to solve advection-dispersion transport equations. *Water Resour. Res.* **28**, 2937–2951.